Evolution of Tsunami-Induced Internal Acoustic–Gravity Waves

CHEN WEI, OLIVER BÜHLER, AND ESTEBAN G. TABAK

Courant Institute of Mathematical Sciences, New York University, New York, New York

(Manuscript received 26 June 2014, in final form 5 February 2015)

ABSTRACT

The authors present an idealized theoretical and numerical study of tsunami-induced internal waves in the atmosphere. These are gravity waves modified by acoustic effects that can propagate rapidly from the ocean surface up to the ionosphere, where they are well known to leave a detectable fingerprint in airglow patterns and other remote sensing observables. Accurate modeling of the wave propagation is a prerequisite for being able to detect and decode this transient observational fingerprint by remote sensing methods. The authors study this problem by formulating the initial-value problem for linear waves forced by an idealized tsunami at the lower boundary and then employing a semianalytic Fourier–Laplace method to solve it. This approach allows them to compute the detailed time evolution of the waves while ensuring that the correct radiation condition in the vertical is satisfied at all times, a nontrivial matter for these transient waves.

The authors also compare the predictions of an anelastic model with that of a fully compressible model in order to discern the importance of acoustic effects. The findings demonstrate that back-reflection at the tropopause is a significant factor for the structure of these waves and that the earliest observable signal in the ionosphere is, in fact, a fast acoustic precursor wave generated by the nearly impulsive formation of the tsunami itself.

1. Introduction

It has been realized since the early days of gravity wave research that vertically propagating gravity waves can provide a very fast mechanism for information transfer across the atmosphere, from ground level all the way up to the ionosphere (Hines 1972), raising the possibility of tsunami detection via gravity wave–induced modulations in the airglow patterns in the ionosphere at roughly 100-km altitude. Of course, this is due to the decay of background atmosphere density with altitude, which increases the amplitude of linear waves by a factor of roughly 3000 between ground level and 100-km altitude. This implies that vertical displacements of only tens of centimeters at the ocean surface can give rise to vertical displacements of hundreds of meters in the ionospheric E region, making possible the detection of tsunamis by monitoring the ionosphere (Peltier and Hines 1976). This theoretical possibility has been confirmed in principle by isolated postevent matching of ionospheric observations with tsunami data (Artru et al. 2005; Rolland et al. 2010; Occhipinti et al. 2011; Makela et al. 2011).

However, current gravity wave modeling approaches based on vertical ray tracing or simple normal mode theory rely on many restrictive assumptions that are simply not satisfied in the real-world complex atmospheric environment. In essence, these approaches reduce the problem to that of stationary mountain lee waves, with the tsunami playing the role of the mountain, a simplicity that comes at a price: 1) considering only stationary solutions omits many observable time-dependent quantitative details associated with the onset of the tsunami; 2) the assumption of only upward-propagating waves does not hold in a nonuniformly stratified atmosphere, where significant partial back-reflection of waves in the vertical naturally occurs, particularly at the tropopause; and 3) compressibility effects are neglected, yet the acoustic component of the signal is significant, due both to the sudden onset of the tsunami and to its fast propagation at roughly two-thirds of the speed of sound.

In this paper, we develop a more complete modeling approach for an idealized two-dimensional setting that captures the wave dynamics in a vertical x–z plane aligned with the tsunami's direction of propagation. The extension to three-dimensional waves is straightforward in principle, though a three-dimensional wave would be

Corresponding author address: Chen Wei, Courant Institute of Mathematical Sciences, New York University, 251 Mercer St., New York, NY 10012.
E-mail: weichen@cims.nyu.edu

DOI: 10.1175/JAS-D-14-0179.1

computationally much more expensive. We find that the nonsatisfaction in the real world of each of the three assumptions above leads to significant effects: the acoustic signal associated with the onset of the tsunami is the first and strongest to arrive at the ionosphere; the subsequent signal is far from stationary for a significant time interval; and the effects of compressibility and wave reflection at the tropopause account for significant changes in both the transient and the asymptotic stationary state.

a. Wave reflection at the tropopause

A standard simplified approach to solve for atmospheric gravity waves generated by a specified vertical displacement at the ground level $\zeta(x, 0, t)$, say, is to use the plane wave structure of vertically upward-propagating waves in order to compute the vertical derivative $\partial_z\zeta(x, 0, t)$ also at the ground level (Occhipinti et al. 2008). Mathematically, this amounts to finding the Dirichlet-to-Neumann map at the ground, under the assumption that the gravity wave field consists exclusively of upward-propagating modes. This is an approximate procedure, because it neglects the partial back-reflections of waves in the vertical, which easily arise in the presence of nonconstant buoyancy frequency. In particular, at the tropopause, the value of buoyancy frequency approximately doubles over a distance of just a few hundred meters, which for the comparatively long vertical waves induced by tsunami means a rapid, nearly discontinuous change. This leads to the back-reflection of a significant portion of the tsunami-induced waves; therefore, the wave structure in the troposphere cannot be approximated well using upward-propagating waves alone. Conversely, solving for the wave field using the simplified approach in the presence of back-reflection at the tropopause leads to unphysical incoming internal waves in the upper atmosphere, which clearly do no satisfy the radiation condition there.

The key factor is to enforce the proper radiation condition in the upper atmosphere as well as the kinematic and dynamic boundary conditions at the tropopause (Nappo 2002, 87–88) in order to achieve a well-posed and correct solution devoid of unphysical waves. We can achieve this in our idealized setting by adapting the recent modeling approach developed in Chumakova et al. (2013), where the wave field is restricted to consist of vertically upward-propagating waves not at the ground, but in the region *above* the tropopause. In the present case, this ensures that the relevant boundary conditions are satisfied in a situation where the buoyancy frequency and wind speed can change discontinuously at the tropopause. This leads to a well-posed problem in which back-reflection is naturally incorporated for both stationary and transient waves.

b. Nonstationarity and compressibility effects

Treating the tsunami as stationary in a moving frame completely neglects both the signal associated with its sudden onset and the transient period of adjustment of the atmospheric wave field to the propagating tsunami. To go beyond these severe limitations, we combine the usual Fourier transform of the governing equations in the horizontal coordinate x with a Laplace transform in time t. This allows us to ascertain the correct causal solution to the initial-value problem for the tsunami-generated internal waves, which in the long run asymptotes toward the stationary solution described by the mountain lee-wave approach.

Yet particularly noteworthy is the existence of a much faster signal arrival in the ionosphere than that of gravity waves. This is the rapid acoustic component of the tsunami-induced waves. To capture this signal, we extend the model beyond the anelastic equations to a fully compressible atmosphere. It turns out that the only extra complexity that this adds to the Laplace-transformed problem is in the expressions for the eigenvalues associated with the boundary value problem, but the structure of this problem remains the same.

c. Plan of the paper

Section 2 sets the scene by studying the anelastic model. After posing the system and reducing it to a single fourth-order equation, we consider a simplified scenario with piecewise constant coefficients, corresponding to two isothermal states with uniform wind, one modeling the troposphere and one the stratosphere and above. We Fourier transform this system in space and Laplace transform it in time, derive the jump conditions at the tropopause, and solve the resulting boundary value problem in closed form. By adopting idealized shapes for the propagating tsunami and for its nearly impulsive onset, the Fourier–Laplace-transformed solution can be found explicitly, although the inverse transforms to recover the solution in physical space must be computed numerically. The numerical inverse Laplace transform is adopted from Brančík (2011). The solution is compared to one without back-reflection at the tropopause and with the more classical stationary solution isomorphic to mountain lee waves. It is found that the existence of back-reflection gives rise to a nontrivial sensitivity of the solution to the tsunami speed: a discrete set of speeds yields waves that resonate with the height of the tropopause, thus creating alternating maxima and minima in the pseudomomentum flux. Also, for speeds above a critical value of roughly 250 m s^{-1} for a realistic atmosphere, the pseudomomentum flux vanishes, with the tsunami yielding evanescent, rather than radiating, waves.

Section 3 extends the analysis by considering a fully compressible atmosphere. Much of the analytical structure of the solution carries through to this more complicated scenario. An interesting modeling issue arises: the full atmosphere can no longer be consistently modeled as two contiguous isothermal layers, since the stratosphere would have to be simultaneously warmer than the troposphere for the tropopause to be convectively stable and colder so as to have higher stratification. We have found an elegant solution to this dilemma: modeling each layer through a system with constant coefficients, as in an isothermal atmosphere, but specifying not the temperature but the lapse rate. We check the accuracy of this approximation by dividing the troposphere into more layers and verifying that the solution changes little.

Section 4 explores the consequences of including compressibility effects. These come in two types: a fast acoustic pulse that carries the first signal of the developing tsunami high into the atmosphere, and a quantitative change present even in the asymptotic stationary regime and that can be partially interpreted using the Prandtl–Glauert factor familiar from compressible airfoil theory (Shapiro 1953), which departs significantly from unity for real tsunamis, which have Mach numbers of roughly two-thirds. Some concluding remarks are offered in section 5.

2. Anelastic fluid model

a. Governing equations for anelastic waves

The target depth of vertical propagation from the sea surface to the ionosphere is about 100 km, which makes modeling the density decay an essential component. The simplest model is therefore a set of anelastic equations, which filters sound waves but accommodates the density decay. We use a very simple version of the anelastic equations, which differs from the standard Boussinesq equations only in the continuity equation. Specifically, we use the two-dimensional linear anelastic equations for a frictionless adiabatic fluid [(18)–(21) in Lipps (1990); (4.1) in Bannon (1996)]:

$$\partial_x(\rho_0 u) + \partial_z(\rho_0 w) = 0, \tag{1a}$$

$$D_t u + U' w + \partial_x(p/\rho_0) = 0, \tag{1b}$$

$$D_t w + \partial_z(p/\rho_0) - b = 0, \quad \text{and} \tag{1c}$$

$$D_t b + N^2 w = 0. \tag{1d}$$

Here $D_t = \partial_t + U\partial_x$, with $U = U(z)$ the background wind, u is the linear perturbation from U, w is the vertical velocity, $\rho_0(z)$ is the background density, p is the linear perturbation from the background pressure, b is the buoyancy disturbance, a prime denotes the vertical derivative of a background field, and $N(z)$ is the buoyancy frequency. The peculiar placement of $\rho_0(z)$ inside the z derivative in the vertical momentum equation is consistent with the definition of the buoyancy disturbance in the presence of a finite density scale height $H(z) = -\rho_0/\rho_0'$. Coriolis forces are neglected, as it will turn out that the internal waves have intrinsic frequencies that are much higher than the Coriolis frequency.

We now derive a single equation for the vertical particle displacement ζ defined by $D_t\zeta = w$. First, we eliminate ρ and u from (1) and obtain

$$D_t^2(\rho_0 w) + N^2\rho_0 w = -D_t\partial_z p - \frac{1}{H}D_t p$$
$$-\partial_x^2 p = -D_t\partial_z(\rho_0 w) + U'\partial_x(\rho_0 w). \tag{2}$$

Second, we rescale ζ and p by

$$\tilde{\zeta} \equiv \sqrt{\rho_0}\zeta \quad \text{and} \quad \tilde{p} \equiv p/\sqrt{\rho_0} \tag{3}$$

and substitute in (2) to obtain

$$(D_t^2 + N^2)\tilde{\zeta} = -\left(\partial_z + \frac{1}{2H}\right)\tilde{p}$$
$$\partial_x^2\tilde{p} = D_t^2\left(\partial_z - \frac{1}{2H}\right)\tilde{\zeta}. \tag{4}$$

Last, by eliminating $\tilde{p}$, we obtain the single equation

$$\left[(D_t^2 + N^2)\partial_x^2 + \left(\partial_z + \frac{1}{2H}\right)D_t^2\left(\partial_z - \frac{1}{2H}\right)\right]\tilde{\zeta} = 0, \tag{5}$$

which has to be augmented with suitable initial and boundary conditions, of course. So far, we allowed for arbitrary coefficients described by background fields (U, N, H) as a function of altitude, but we now restrict to two layers with piecewise constant sets of coefficients, one for the troposphere and one for the rest of the atmosphere, which includes the stratosphere. Physically, this corresponds to an isothermal background state within each layer.

b. Solution with piecewise constant coefficients

We use subscripts 1 and 2 to denote quantities in the troposphere and the air above, respectively, and use z_p for the height of tropopause that separates the two regions. Within these regions (U, N, H) are constant; hence, (5) simplifies to ($i = 1, 2$):

$$(\partial_t + U_i\partial_x)^2\left(\partial_x^2 + \partial_z^2 - \frac{1}{4H_i^2}\right)\tilde{\zeta}_i + N_i^2\partial_x^2\tilde{\zeta}_i = 0. \tag{6}$$

We assume zero initial conditions for $\tilde{\zeta}_i(x, z, t)$: that is,

$$\tilde{\zeta}_i(x, z, 0) = \partial_t\tilde{\zeta}_i(x, z, 0) = 0. \tag{7}$$

We apply a Fourier transform in x and a Laplace transform in t to (6), and, using (7), we obtain its transformed counterpart:

$$\partial_z^2 \hat{\zeta}_i^{\mathrm{T}} = \left[\frac{k^2 N_i^2}{(s+ikU_i)^2} + k^2 + \frac{1}{4H_i^2} \right] \hat{\zeta}_i^{\mathrm{T}} \tag{8}$$

for $\hat{\zeta}_i^{\mathrm{T}}(k, z, s)$. Here, $\widehat{(\cdot)}(k, \cdot)$ denotes the Fourier transform in x, and $(\cdot)^{\mathrm{T}}(\cdot, s)$ denotes the Laplace transform in t. For fixed k and s, this is a second-order ODE in z in each of the two regions; therefore, four boundary conditions in z are required to determine $\hat{\zeta}_1^{\mathrm{T}}(k, z, s)$ and $\hat{\zeta}_2^{\mathrm{T}}(k, z, s)$ uniquely.

At the sea level $z = 0$ we have the kinematic boundary condition $\tilde{\zeta} = \sqrt{\rho_0(0)}h$, where $h(x, t)$ is a given function that describes the ocean tsunami motion. This yields

$$\hat{\zeta}_1^{\mathrm{T}}(k, 0, s) = \sqrt{\rho_0(0)}\hat{h}^{\mathrm{T}}(k, s). \tag{BC1}$$

For the initial-value problem that we are envisaging, the correct boundary condition at infinite altitude is $\tilde{\zeta} = 0$, which yields

$$\hat{\zeta}_2^{\mathrm{T}}(k, \infty, s) = 0. \tag{BC2}$$

The kinematic and dynamic boundary condition at the tropopause $z = z_p$ are that the vertical displacement and the total pressure are continuous across the undulating tropopause in a manner that is familiar from solving for interfacial waves between fluid layers of unequal density. However, the present situation is somewhat simpler, because the background density and therefore the background pressure gradient due to hydrostatic balance are continuous across the tropopause. First, the kinematic condition obviously implies

$$\hat{\zeta}_1^{\mathrm{T}}(k, z_p, s) = \hat{\zeta}_2^{\mathrm{T}}(k, z_p, s). \tag{BC3}$$

Second, the dynamic pressure condition reduces to continuity of the perturbation pressure $\tilde{p}$, which by the second equation in (4) implies

$$[D_t^2 \partial_z \tilde{\zeta}]_{z_p-}^{z_p+} = \left[\frac{D_t^2 \tilde{\zeta}}{2H} \right]_{z_p-}^{z_p+}.$$

After the Fourier–Laplace transform, this gives

$$[(s+ikU)^2 \partial_z \hat{\zeta}^{\mathrm{T}}]_{z_p-}^{z_p+} = \left[\frac{(s+ikU)^2 \hat{\zeta}^{\mathrm{T}}}{2H} \right]_{z_p-}^{z_p+}. \tag{BC4}$$

A lengthy but straightforward derivation then yields the solution as

$$\begin{aligned} \hat{\zeta}_1^{\mathrm{T}}(k, z, s) &= \sqrt{\rho_0(0)}\hat{h}^{\mathrm{T}}(k, s) \times \frac{\mu(k,s)\sinh[\lambda_1(k,s)(z_p - z)] + \cosh[\lambda_1(k,s)(z_p - z)]}{\mu(k,s)\sinh[\lambda_1(k,s)z_p] + \cosh[\lambda_1(k,s)z_p]} \\ \hat{\zeta}_2^{\mathrm{T}}(k, z, s) &= \frac{\sqrt{\rho_0(0)}\hat{h}^{\mathrm{T}}(k, s) e^{-\lambda_2(k,s)(z - z_p)}}{\mu(k,s)\sinh[\lambda_1(k,s)z_p] + \cosh[\lambda_1(k,s)z_p]}, \end{aligned} \tag{9}$$

with

$$\lambda_i(k, s) = \sqrt{\frac{k^2 N_i^2}{(s+ikU_i)^2} + k^2 + \frac{1}{4H_i^2}} \quad \text{and} \tag{10a}$$

$$\mu(k, s) = \frac{A_2(k, s) - A_1(k, s) + \lambda_2(k, s)B_2(k, s)}{\lambda_1(k, s)B_1(k, s)}. \tag{10b}$$

Here, λ_i are chosen with the positive real parts, and

$$A_i(k, s) = \frac{(s+ikU_i)^2}{2H_i}, \quad B_i(k, s) = (s+ikU_i)^2. \tag{11}$$

Notably, this solution still allows for different wind speed $U_{1,2}$ in the two layers. The physical wave field $\zeta(x, z, t)$ is obtained from inverting (9):

$$\zeta_i(x, z, t) = \frac{\tilde{\zeta}_i(x, z, t)}{\sqrt{\rho_0(z)}} = \frac{1}{\sqrt{\rho_0(z)}} \mathscr{F}^{-1}[\mathscr{L}^{-1}(\hat{\zeta}_i^{\mathrm{T}})](x, z, t), \tag{12}$$

where $\mathscr{F}^{-1}$ and $\mathscr{L}^{-1}$ denote the inverse Fourier and Laplace transform respectively. In our numerical examples, we choose very idealized functions $h(x, t)$ such that $\hat{h}^{\mathrm{T}}(k, s)$ can be found analytically, but, in any case, the inverse Fourier and Laplace transforms in (12) have to be performed numerically.

c. Idealized setup and lee-wave theory

We set the tropopause height at $z_p = 10\,\mathrm{km}$ and use typical tropospheric and stratospheric values for N and H: $N_1 = 0.01\,\mathrm{s}^{-1}$, $H_1 = 9\,\mathrm{km}$; $N_2 = 0.02\,\mathrm{s}^{-1}$, $H_2 = 6\,\mathrm{km}$. We allowed piecewise constant wind in our equations,

but from now on we consider only the case of no background wind (i.e., $U_1 = U_2 = 0$).

Our idealized model for the tsunami elevation at the sea surface $h(x, t)$ is as follows: in the first phase of duration τ, the elevation $h(x, t)$ grows linearly in time until it reaches a prescribed shape $f(x)$, say. This models the active underwater earthquake and the concomitant near-impulsive deformation of the sea surface into the shape $f(x)$. In the second phase, this shape then simply travels horizontally to the right with a constant speed of propagation V, which models the external wave speed $\sqrt{gH_o}$, where H_o is the ocean depth. For example, if $H_o = 4\,\mathrm{km}$, then $V = 200\,\mathrm{m\,s^{-1}}$.

Of course, this ignores the equal-and-opposite propagation of another tsunami shape to the left, which could trivially be added by linear superposition. As the internal waves stay sharply localized above the moving tsunami source, we find that this makes little difference in practice, so for clarity we focus on the right-going tsunami only. We therefore have

$$h(x,t) = \begin{cases} (t/\tau) f(x), & 0 < t \le \tau \\ f[x - V(t-\tau)], & t > \tau. \end{cases} \tag{13}$$

The transform of $h(x, t)$ is (cf. appendix A)

$$\hat{h}^{\mathrm{T}}(k,s) = e^{-s\tau}\left[\frac{2e^{(s\tau/2)}\sinh(s\tau/2)}{s^2\tau} - \frac{1}{s} + \frac{1}{s+ikV}\right]\hat{f}(k).$$

The tsunami shape is idealized as a Gaussian bump $f(x) = \exp(-x^2/2\sigma^2)$, where $\sigma = 20\,\mathrm{km}$. It is shown in appendix B that this leads to a typical horizontal wavelength of size

$$\lambda_x = 2\pi^{3/2}\sigma \approx 200\,\mathrm{km}. \tag{14}$$

The numerical domain length was 6400 km in the horizontal, which was sufficient to make boundary effects negligible.

One objective of our numerical examples is to show the significance of back-reflection at the tropopause interface, and, for ease of comparison, we therefore also run a reflection-free setup in which the parameter values of the upper layer are extended to the lower layer as well, so N and H are constant throughout and equal to their stratospheric values. Now the natural reference solution is the steady-state solution that is established a long time after the tsunami has been created. As argued in Peltier and Hines (1976), this steady-state solution is equivalent to the familiar lee-wave problem, where the effective wind speed is equal to $-V$. This can be analyzed with elementary wave theory and group-velocity concepts. For example, the dispersion relation linking (k, m) and the intrinsic frequency $\hat{\omega}$ is

$$m^2 = k^2\left(\frac{N^2}{\hat{\omega}^2} - 1\right) - \frac{1}{4H^2}. \tag{15}$$

Using the condition of zero absolute frequency $\hat{\omega}^2 = V^2k^2$, this yields

$$m^2 = \frac{N^2}{V^2} - k^2 - \frac{1}{4H^2} \approx \frac{N^2}{V^2} \tag{16}$$

for the vertical wavenumber m. The indicated rough approximation is valid because, for our choice of $f(x)$, the relevant range of horizontal wavenumbers is $|k| \le 1/\sigma$, which makes the other two terms comparable in size but small compared to the first term. Hence, the expected vertical wavelength is approximately

$$\lambda_z = \frac{2\pi}{|m|} = \frac{2\pi V}{N} \approx 60\,\mathrm{km}. \tag{17}$$

These are therefore very deep waves, with a vertical wavelength that is some 10 times larger than the familiar mountain lee waves, because the effective wind speed is 10 times larger. Under the approximation in (16), the size of the vertical group velocity $w_g = \partial\hat{\omega}/\partial m$ is easily computed and takes the form

$$|w_g| = V^2\frac{|k|}{N} = V\,\frac{|\hat{\omega}|}{N} \approx 50 - 100\,\mathrm{m\,s^{-1}}. \tag{18}$$

The first expression shows that, for fixed k, the group velocity is proportional to V^2, while the second expression makes obvious that V is an upper bound for w_g. For fixed V and $f(x)$, we have that small-scale horizontal features travel fastest in the vertical; for the envisaged parameter values, we get the indicated range of w_g, which shows that tsunami-induced internal waves can travel to the ionosphere at 100-km altitude in less than an hour.

d. *Numerical examples, back-reflection, and tsunami speed*

Figure 1 shows two snapshots of the scaled vertical displacement $\tilde{\zeta}$ at time $t = 40\,\mathrm{min}$ for $V = 200\,\mathrm{m\,s^{-1}}$, which is the speed of a tsunami on an ocean with depth of $H_o = 4\,\mathrm{km}$; there is also a third snapshot at time $t = 5\,\mathrm{min}$ for comparison with the later compressible model. The plots are centered over the current position of the tsunami, and the hydrostatic part of the wave field remains on top of the tsunami, while the nonhydrostatic part of the wave field lags behind, which is a scenario that is familiar from mountain lee waves. These plots also illustrate that smaller horizontal scales travel faster than larger horizontal scales, which is consistent with (18). Moreover, the left panel is the control run without a tropopause, which clearly shows significantly higher

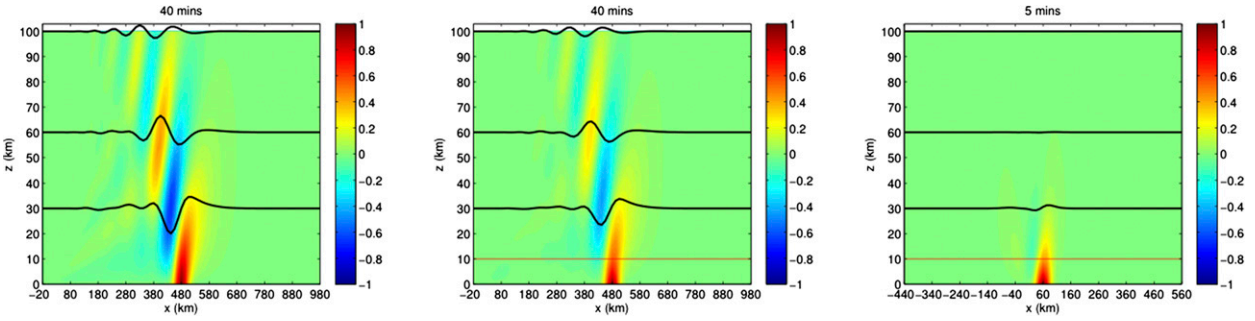

FIG. 1. Snapshots of scaled vertical displacement $\tilde{\zeta}$ in the anelastic model for $V = 200\,\mathrm{m\,s^{-1}}$. Also shown are three line plots defined by $z + 15\,000 \times \tilde{\zeta}(x, z, t)$, with $z \in \{30, 60, 100\}$ km, respectively. These are material lines with greatly exaggerated deformations, and they illustrate that shorter scales travel faster than longer scales. (left) Uniform stratification at $t = 40$ min; (middle) with tropopause located at $z = 10$ km; (right) with tropopause, but at earlier time $t = 5$ min.

wave amplitudes than the run with a tropopause on the right. The size of the amplitude difference turns out to be a sensitive function of the tsunami speed V.

This is illustrated in Fig. 2, which shows the time history of the horizontally averaged root-mean-square value of scaled vertical displacement at altitude 100 km for three different speeds V. The plotted displacement amplitude has been normalized by the amplitude of the topography shape $f(x)$. In the left panel, the speed is very low (viz. just $V = 30\,\mathrm{m\,s^{-1}}$), and there is little difference between the wave field with or without the tropopause jump. This is the familiar situation from topographic gravity wave parameterization schemes, where near-surface winds are a few tens of meters per second at most, and where back-reflection is typically ignored. The situation changes significantly in the middle panel, where $V = 100\,\mathrm{m\,s^{-1}}$. Here, the uniformly stratified case exhibits significantly higher (almost double) asymptotic wave amplitude than the case with a tropopause, which indicates that significant back-reflection is taking place there. Comparing with the left panel, we can also see that the faster horizontal tsunami speed results in faster vertical propagation of the internal waves, as predicted by (18). Finally, the right panel is based on $V = 200\,\mathrm{m\,s^{-1}}$. Again, the inclusion of the tropopause is clearly significant.

At this point, it seems that speeds below $V = 30\,\mathrm{m\,s^{-1}}$ are unaffected by the tropopause, but this is actually not the case. One easy way to show this is presented in the left panel in Fig. 3, which shows the steady-state vertical flux of horizontal pseudomomentum [divided by $\rho_0(0)$]:

$$D = -\overline{u'w'} \quad \text{at} \quad z = 0. \tag{19}$$

The size of the pseudomomentum flux is a good indicator for the importance of back-reflection, as, without reflection, the lee-wave pseudomomentum flux takes the simple shape indicated by the blue line in the left panel. By contrast, the red line shows the pseudomomentum flux after including the tropopause, which has a complicated oscillatory structure for speeds below $V = 50\,\mathrm{m\,s^{-1}}$ and remains below the blue curve at higher speeds. This shows that the agreement for $V = 30\,\mathrm{m\,s^{-1}}$ in the previous figure was fortuitous, and

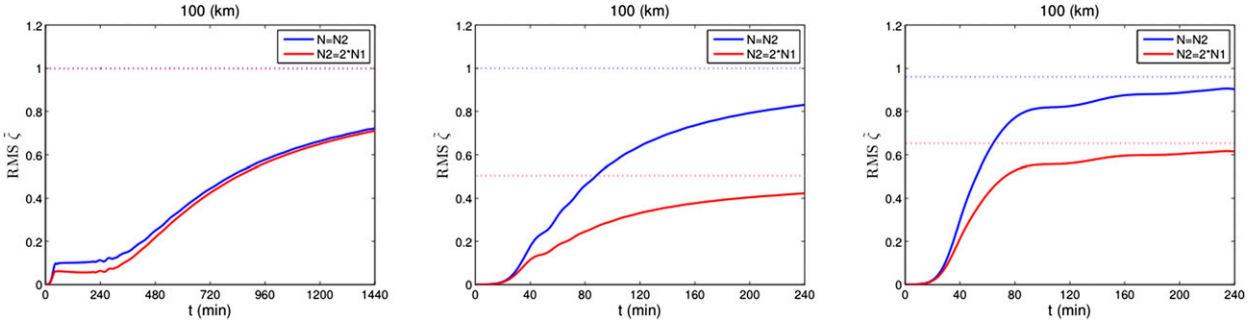

FIG. 2. Time evolution of anelastic gravity wave amplitudes at $z = 100$ km with a tropopause (red line) and without (blue line). The tsunami speeds across the panels are (left) $V = 30$, (middle) $V = 100$, and (right) $V = 200\,\mathrm{m\,s^{-1}}$; and the stippled lines indicate the asymptotic steady-state limit; note the much longer integration time for $V = 30\,\mathrm{m\,s^{-1}}$. In the $V = 200\,\mathrm{m\,s^{-1}}$ case, the uniformly stratified limit is less than unity, because part of the wave field is evanescent.

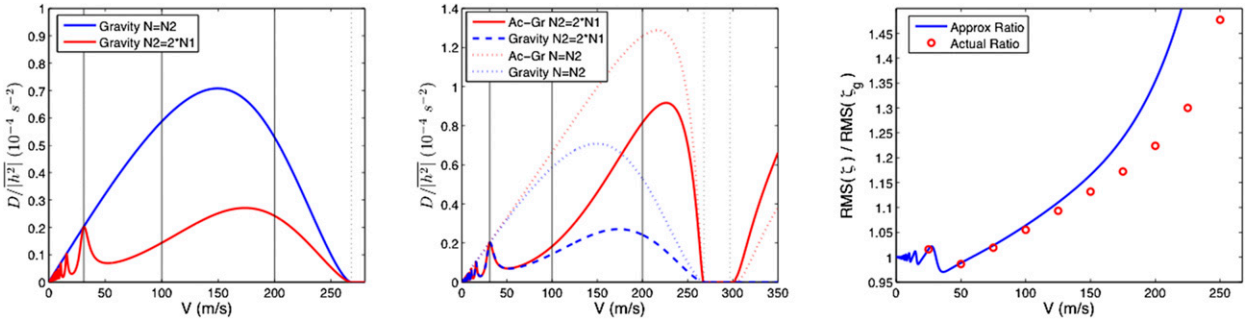

FIG. 3. (left) Pseudomomentum flux D as a function of V in anelastic model with and without a tropopause. (middle) Pseudomomentum flux D for larger range of V and for both anelastic and compressible models with and without a tropopause. The forbidden tsunami speed zone is clearly visible. (right) Root-mean-square ratio of acoustic–gravity waves to anelastic gravity waves in case with tropopause. The red circles are the actual ratios, and the blue solid line is the scaled pseudomomentum flux ratio $\sqrt{\beta^2 D/D_g}$, which crudely measures the increased back-reflection in the anelastic case. Without a tropopause, this scaled pseudomomentum flux ratio would be unity by (33).

back-reflection may be relevant even for the comparatively small wind speeds typical for mountain-wave generation and parameterizations in GCMs.

We find that, for certain values of V in the low-speed range, the pseudomomentum flux does not depend on whether the stratification is constant or not. For example for the speed $30\,\mathrm{m\,s^{-1}}$, the pseudomomentum fluxes are the same, and, correspondingly, the wave fields are also the same. Interestingly, for this speed, half the vertical wavelength fits into the troposphere, a situation that is not possible at higher speeds but occurs for many lower speeds, as indicated in the figure. This indicates a resonance condition between the vertical wave structure and the tropopause height.

Another observation of Fig. 3 is that, for anelastic waves, there is a speed barrier of $268\,\mathrm{m\,s^{-1}}$ for the pseudomomentum flux such that, when the tsunami travels faster than this speed, there is no pseudomomentum flux into the stratosphere, and thus the wave field above the tropopause is evanescent. Indeed, this is the reason why the asymptotic amplitude for the blue line in the right panel of Fig. 2 falls short of unity: some horizontal wavenumbers are already evanescent for this high tsunami speed. In summary, if we model gravity waves as anelastic, the effect of stratification is significant for fast-moving lower boundaries of speeds 50–$250\,\mathrm{m\,s^{-1}}$ in the open ocean, except for some slow speeds no greater than $30\,\mathrm{m\,s^{-1}}$ whose induced vertical wavelength fits the troposphere.

The present anelastic model suffers from several shortcomings in the tsunami problem. For example, the Mach number based on the tsunami speed V for a realistic ocean depth is about $\frac{2}{3}$, which is not small. This makes dynamic compressibility relevant, an effect that is missing from the anelastic continuity equation. Moreover, even for smaller speeds V, the anelastic model is unrealistic for the very early stage of the wave propagation, which is relevant for discerning the precise nature of the first-arrival signal at the ionosphere. This is due to the action-at-a-distance property that the anelastic equations share with the familiar Boussinesq equations: in these models the sound speed is effectively infinite, and signals may get transmitted instantaneously. For example, as shown in appendix D, the anelastic response in terms of the Fourier-transformed vertical displacement $\hat{\zeta}$ to an impulsively started tsunami has a vertical structure that decays as $\exp(-\lambda z)$ where

$$\lambda = \sqrt{k^2 + \frac{1}{4H_2^2}} - \frac{1}{2H_2}. \tag{20}$$

This means that the ionosphere at $z = 100\,\mathrm{km}$ is instantaneously disturbed by the creation of the tsunami at sea level, which is unphysical. Of course, the size of the impulsive disturbance decays with altitude, but the decay rate implied by (20) is actually quite modest if $k^2 \sim 1/\sigma^2$, with an implied e-folding length of about $20\,\mathrm{km}$ or more. Indeed, we have found that plots analogous to the left and middle panels in Fig. 1 but taken at lower altitude were noticeably affected by the spurious instantaneous response at early times. Even though this response is quite small in the high altitudes and does not affect significantly the ionospheric signal, this spurious instantaneous response has been created throughout the atmosphere because of anelasticity. This fact, together with the inevitability of finite Mach number effects, calls for the use of a fully compressible model, as in Peltier and Hines (1976), which we pursue next.

3. Compressible fluid model

The fully compressible fluid model allows for acoustic–gravity waves, has no spurious action-at-a-distance effects, and can deal with the high Mach numbers associated with the tsunami speed V. In particular, the inclusion of realistic acoustic waves for the initial-value problem is important, because observations show that the first arrival of a transient signal of tsunami-induced waves occurs at 100-km altitude just 5 min after the tsunami is generated. This fast and transient response is clearly acoustic in nature. We find that the structure of the asymptotic, steady-state wave field also differs noticeably from the anelastic case, which is because of the high Mach number of about 2/3.

a. Governing equations for compressible waves

We use the equations for a linearized stratified compressible adiabatic fluid in the form

$$D_t\rho + \rho_0(\partial_x u + \partial_z w) + \rho_0' w = 0, \tag{21a}$$

$$\rho_0(D_t u + U'w) + \partial_x p = 0, \tag{21b}$$

$$\rho_0 D_t w + \partial_z p + g\rho = 0, \tag{21c}$$

$$D_t p + p_0' w - c^2(D_t\rho + \rho_0' w) = 0, \quad \text{and} \tag{21d}$$

$$p_0' + \rho_0 g = 0. \tag{21e}$$

The notation is the same as before, with additional symbols for the background pressure p_0 and the background sound speed:

$$c^2 = \gamma\frac{p_0}{\rho_0} = \gamma R T_0. \tag{22}$$

Here, γ is the ratio of the specific heats, R is the gas constant, and T_0 is background temperature. The buoyancy frequency is now defined as

$$N^2 = \frac{g}{H} - \frac{g^2}{c^2} \quad \text{and} \quad H = -\frac{\rho_0}{\rho_0'}, \tag{23}$$

as before. If the lapse rate is defined by $\Gamma = -T_0'$, then the profiles of (N, H, c, T_0) are linked by (22) as well as

$$H = \frac{RT_0}{g - \Gamma R} \quad \text{and} \quad N^2 = \frac{g^2}{RT_0}\left(\frac{\gamma - 1}{\gamma} - \frac{\Gamma R}{g}\right). \tag{24}$$

Eliminating ρ and u from (21), we obtain a complete set of equations for $\rho_0 w$ and p:

$$\begin{aligned} D_t^2(\rho_0 w) + N^2\rho_0 w &= -\frac{g}{c^2}D_t p - D_t\partial_z p \\ D_t^2 p - c^2\partial_x^2 p &= -\frac{c^2N^2}{g}D_t(\rho_0 w) - c^2 D_t\partial_z(\rho_0 w) \\ &\quad + c^2 U'\partial_x(\rho_0 w). \end{aligned} \tag{25}$$

Applying the rescaling (3) again turns (25) into

$$\begin{aligned} (D_t^2 + N^2)\tilde{\zeta} &= \left(\frac{1}{2H} - \frac{g}{c^2} - \partial_z\right)\tilde{p} \\ (D_t^2 - c^2\partial_x^2)\tilde{p} &= c^2 D_t^2\left(\frac{1}{2H} - \frac{N^2}{g} - \partial_z\right)\tilde{\zeta}. \end{aligned} \tag{26}$$

This is a complicated set of equations, although, in the special case of constant U and T_0, this set has constant coefficients and therefore admits plane acoustic–gravity waves with the celebrated dispersion relation

$$m^2 = \frac{\hat{\omega}^2}{c^2} + k^2\left(\frac{N^2}{\hat{\omega}^2} - 1\right) - \frac{1}{4H^2}. \tag{27}$$

The compressible term $\hat{\omega}^2/c^2$ always increases the value of m^2 over its anelastic value, and, for the lee-wave problem, the relative magnitude of this increase can be estimated as $(\hat{\omega}^2/N^2)(V^2/c^2)$, which exhibits the importance of the Mach number squared.

Returning to the general equation (26), we cannot simply eliminate $\tilde{p}$ in the physical space variables, because the operators on $\tilde{p}$ do not commute. But if we apply the Fourier–Laplace transform and use homogeneous initial conditions for $\tilde{\zeta}$ and $\tilde{p}$ and their time derivatives, then we are able to obtain a single equation for the transformed variable $\hat{\zeta}^{\mathrm{T}}(k, z, s)$:

$$[(s + ikU)^2 + N^2]\hat{\zeta}^{\mathrm{T}} = \left(\partial_z + \frac{g}{c^2} - \frac{1}{2H}\right)\frac{c^2(s + ikU)^2}{(s + ikU)^2 + c^2k^2}\left(\partial_z + \frac{N^2}{g} - \frac{1}{2H}\right)\hat{\zeta}^{\mathrm{T}}. \tag{28}$$

b. Modeling the troposphere and tropopause

Peltier and Hines (1976) computed the steady-state wave pattern based on a completely isothermal atmosphere, which admits simple plane wave solutions with the dispersion relation (27). We seek to model the tropopause and the positive jump in N^2 across it, but it is not possible to do this by simply adjoining two isothermal

layers because of convective instability. This is easy to see from (24) with zero lapse rate $\Gamma = 0$. Then, if N increases across a tropopause jump, it follows that T_0 must decrease, and pressure continuity then implies that ρ_0 *increases* across the tropopause. This means the background state would be unstable.

In the real atmosphere, the lower value of N_1 in the troposphere is associated with the nonzero lapse rate $\Gamma_1 \approx 7\,\mathrm{K\,km^{-1}}$ there, while $\Gamma_2 \approx 0$ to first approximation in the stratosphere. We therefore proceed by adopting a simple two-layer model that uses these two lapse rates but ignores the vertical variations of temperature in the two layers. Specifically, we use $T_1 = 218\,\mathrm{K}$ in the upper layer and a midtropospheric value $T_1 = 254\,\mathrm{K}$ in the lower layer; the corresponding sound speeds are $c_2 \approx 296\,\mathrm{m\,s^{-1}}$ and $c_1 \approx 320\,\mathrm{m\,s^{-1}}$. The values for H and N in the two layers are then the same as for the anelastic model: $N_1 = 0.01\,\mathrm{s^{-1}}$, $H_1 = 9\,\mathrm{km}$; $N_2 = 0.02\,\mathrm{s^{-1}}$, $H_2 = 6\,\mathrm{km}$. Of course, this simplistic approach ignores variations in T_0 and the other fields of some 10%–20% in the troposphere. To check how sensitive our results are, we have also formulated a more complicated multilayer model, which is described in section 3c below.

We now substitute piecewise constant (N, H, c, U) into (28) and obtain

$$\partial_z^2 \hat{\zeta}_i^{\mathrm{T}} = \left\{ \left(\frac{1}{2H_i} - \frac{N_i^2}{g} \right)^2 + \frac{[(s+ikU_i)^2 + N_i^2][(s+ikU_i)^2 + c_i^2 k^2]}{c_i^2 (s+ikU_i)^2} \right\} \hat{\zeta}_i^{\mathrm{T}}, \tag{29}$$

to be solved in two layers indexed by the subscript $i \in \{1, 2\}$. This requires four boundary conditions, and the first three boundary conditions are the same as (BC1)–(BC3). The jump condition for the vertical gradient of vertical displacement is slightly modified. Integrating (28) from z_p^- to z_p^+, we obtain the jump condition:

$$\left[\frac{c^2 (s+ikU)^2}{(s+ikU)^2 + c^2 k^2} \partial_z \hat{\zeta}^{\mathrm{T}} \right]_{z_p^-}^{z_p^+} = \left[\frac{c^2 (s+ikU)^2}{(s+ikU)^2 + c^2 k^2} \left(\frac{1}{2H} - \frac{N^2}{g} \right) \hat{\zeta}^{\mathrm{T}} \right]_{z_p^-}^{z_p^+} \tag{BC4′}$$

The solution of (29) with boundary conditions (BC1)–(BC3) and (BC4′) is given by (9) with

$$\lambda_i(k,s) = \sqrt{\left(\frac{1}{2H_i} - \frac{N_i^2}{g} \right)^2 + \frac{[(s+ikU_i)^2 + N_i^2][(s+ikU_i)^2 + c_i^2 k^2]}{c_i^2 (s+ikU_i)^2}}$$
$$\mu(k,s) = \frac{A_2(k,s) - A_1(k,s) + \lambda_2(k,s) B_2(k,s)}{\lambda_1(k,s) B_1(k,s)}, \tag{30}$$

where the λ_i are chosen with the positive real parts, and

$$A_i(k,s) = \frac{c_i^2 (s+ikU_i)^2}{(s+ikU_i)^2 + c_i^2 k^2} \left(\frac{1}{2H_i} - \frac{N_i^2}{g} \right)$$
$$B_i(k,s) = \frac{c_i^2 (s+ikU_i)^2}{(s+ikU_i)^2 + c_i^2 k^2}. \tag{31}$$

As in the anelastic case, in our numerical examples below, we will use zero winds so we set $U_i = 0$ from now on.

The asymptotic steady-state limit of the isothermal fully compressible model is the same as the one proposed by Peltier and Hines (1976). We see, from the comparison of the asymptotic steady-state limits of the nonisothermal model with the isothermal one in Fig. 4, that including the tropopause reduces the wave amplitude in the long run. This makes the back-reflection at the tropopause a significant factor in the modeling of acoustic–gravity waves.

c. *Multilayer modeling of the troposphere*

We have analytically solved the equations at the price of approximating the linear temperature profile of the troposphere by the temperature in the middle of that layer so as to have constant coefficients in the equations. To improve on this shortcoming, we can model the troposphere using several layers (i.e., we allow a number of n layers in the troposphere). For the ith layer from the bottom, we have $T_1^{(i)} = T[(i-0.5)z_p/n] = T(0) - \Gamma(i-0.5)z_p/n$; consequently, $N_1^{(i)} = \sqrt{(g/c_p - \Gamma)g/T_1^{(i)}}$, $H_1^{(i)} = T_1^{(i)}/(g/R - \Gamma)$, and $c_1^{(i)} = \sqrt{\gamma R T_1^{(i)}}$, where c_p is the specific heat capacity. We then need to solve $n + 1$ eigenvalue problems (including the one in the stratosphere), which are formally the same as the ones in (29), for $2n + 2$ unknown coefficients of eigenfunctions, where the eigenfunctions and the eigenvalues are known a priori. We have $n - 1$ kinematic boundary conditions and $n - 1$ dynamic boundary conditions between the semi-isothermal layers; we have one

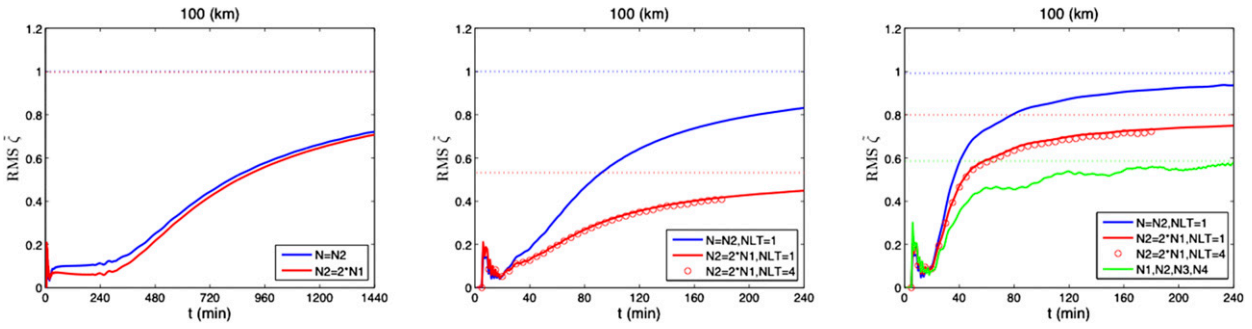

FIG. 4. As in Fig. 2, but for compressible acoustic gravity waves. In the first 5–10 min, a signal due to a fast acoustic precursor wave is clearly visible. The plots also indicate that our results are insensitive to the value of the number of tropospheric layers used in the numerical model (NLT), see section 3c. The blue dotted lines indicate the asymptotic steady-state limit of the isothermal fully compressible model, in agreement with the one proposed by Peltier and Hines (1976). Compared to Fig. 2, the evanescent part of the compressible wave field is much weaker at $V = 200\,\mathrm{m\,s^{-1}}$, and hence the asymptotic amplitude in the uniformly stratified case is almost unity. (right) The green lines are the solutions with a more realistic atmospheric profile summarized in Table 1. This solution is qualitatively similar to the one plotted in red lines, but with a smaller amplitude, due mostly to partial reflection around the mesopause and to the larger rigidity (i.e., smaller density scale height H) above the mesosphere.

kinematic boundary condition and one dynamic boundary condition between the top layer of the troposphere and the stratosphere; we have one boundary condition at the sea level and one boundary condition at infinite altitude. In total, we have $2(n-1)+2+2=2n+2$ boundary conditions for $2n+2$ unknown coefficients. This yields a solvable $(2n+2)\times(2n+2)$ linear system.

We have compared our standard $n=1$ model with results based on a model with $n=4$ layers in the troposphere and found very encouraging agreement. For example, the circles plotted in Fig. 4 are based on the $n=4$ model, and they compare very well with the lines based on the $n=1$ model. We therefore believe that the simple two-layer model is capable of capturing the essence of the tsunami-induced acoustic–gravity waves.

4. Fast and slow compressible effects

Both the slow, steady-state lee waves, as well as the fast, transient initial wave field are significantly altered by the inclusion of compressible effects. The slow effects are most easily discussed in terms of the steady-state pseudomomentum flux and the establishment of the vertical displacement at different altitudes. Here, the similarity with the anelastic results depends greatly on the tsunami speed V, as expected. The new fast effects are dominated by an acoustic pulse that crosses the atmosphere in a few minutes and is the first signal to arrive at the ionosphere. Notably, this acoustic pulse was entirely absent in the anelastic system.

a. *Prandtl–Glauert factor, pseudomomentum flux, and amplitude*

The steady-state pseudomomentum flux for anelastic waves in a uniformly stratified atmosphere is [cf. (C1)]

$$D_g = \sum_{k\in S} kV^2 m_g(k)|\hat{\zeta}(k)|^2, \tag{32}$$

where m_g is taken from the equality in (16), and S is the set of k such that the corresponding wave modes are propagating waves (i.e., $m_g^2>0$). Here and below we will use the subscript g to denote anelastic gravity waves. By comparison, the pseudomomentum flux for acoustic–gravity waves is [cf. (C2)]

$$D = \frac{\sum_{k\in S} kV^2 m(k)|\hat{\zeta}(k)|^2}{1-(V/c)^2} \approx \frac{D_g}{\beta^2}, \tag{33}$$

where by (27) the wavenumber m now follows from $m^2 = m_g^2 + V^2k^2/c^2$. This is a modest change, so $m(k)\approx m_g(k)$ to good approximation. Equation (33) for the pseudomomentum flux highlights the importance of the so-called Prandtl–Glauert factor:

$$\beta \equiv \sqrt{1-\frac{V^2}{c^2}} \le 1, \tag{34}$$

which was first introduced in the context of compressible airfoil theory. It makes it obvious that, in a uniformly stratified atmosphere, the pseudomomentum flux is increased by a factor of $1/\beta^2$ when compressibility is taken into account. If a tropopause is included, then these formulas can be adapted to hold in the upper layer, where all waves are propagating upward, but $\hat{\zeta}(k)$ in the upper layer is then, of course, not known a priori. The results of computing the pseudomomentum flux numerically in all cases as a function of V are shown in the middle panel of Fig. 3. Broadly speaking, differences between the anelastic and compressible

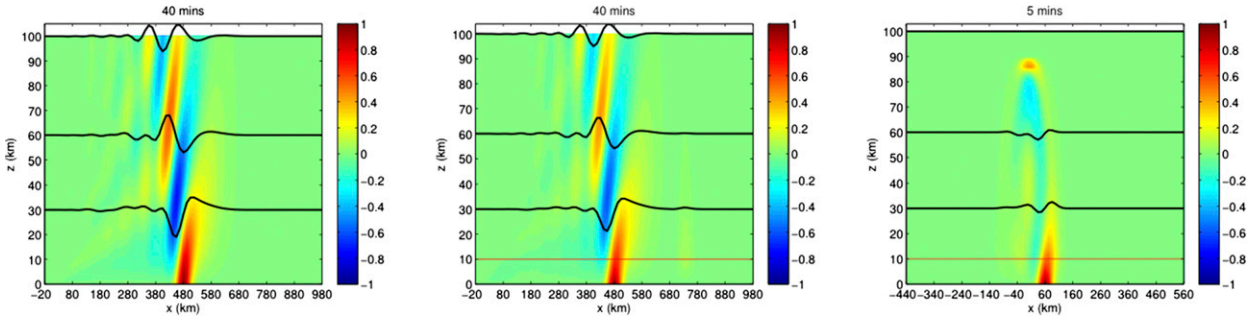

FIG. 5. As in Fig. 1, but for the compressible model. (left) Uniform stratification at $t = 40$ min; (middle) with tropopause; (right) with tropopause at $t = 5$ min, showing a fast acoustic precursor wave that is clearly absent in Fig. 1.

pseudomomentum flux become significant for speeds larger than $V = 100\,\mathrm{m\,s^{-1}}$.

The main steady-state observable is not the pseudomomentum flux, of course, but the vertical displacement. In the case of uniform stratification the root-mean-square value of the scaled vertical displacement is in fact the same in the anelastic and compressible models, because it has to be equal to the root-mean-square value of the tsunami shape $f(x)$. So in this case increased pseudomomentum flux does not translate into increased vertical displacement.

The situation is different once a tropopause is included, in which case compressibility tends to increase vertical displacement as well as pseudomomentum flux, but the former increase is less pronounced than the latter. This is illustrated in the right panel of Fig. 3, which shows the ratio of compressible to anelastic displacement amplitudes as a function of V in a case with a tropopause. Physically, the interpretation is that back-reflection at the tropopause is stronger in the anelastic model than in the compressible model.

b. *Forbidden tsunami speeds for propagating waves*

The middle panel of Fig. 3 also makes conspicuous that there are speeds V for which there are no propagating waves at all. This is easily understood from (27), from which the condition for propagating lee waves follows as

$$m^2(k) = \frac{N^2}{V^2} - \frac{1}{4H^2} - k^2\left[1 - \left(\frac{V}{c}\right)^2\right] > 0. \qquad (35)$$

If $2NH < V < c$, then this is never satisfied, regardless of the values of k. But for $V < 2NH$ or $V > c$, there always exists a k such that $m^2(k)$ is nonnegative. Therefore, the forbidden tsunami speeds for acoustic–gravity waves are $2NH < V < c$. The anelastic version of this result is $2NH < V$. It is noteworthy from the forbidden tsunami speeds that, for a subsonic tsunami, there is a speed barrier $2N_2H_2 \approx 268\,\mathrm{m\,s^{-1}}$ such that, if the tsunami travels faster than this speed, then there are no propagating waves into the stratosphere, no matter whether the atmosphere is uniformly stratified or not and no matter whether compressible effects are included.

c. *Time-dependent amplitude and fast acoustic precursor wave*

Figure 4 shows the same vertical displacement diagnostic as in the earlier Fig. 2, but this time for compressible waves. (The figure also shows a successful cross-check of our numerical method against a simulation with more layers in the troposphere.) At long times the structure of the anelastic and the compressible curves is similar though not identical; for example, overall there seems to be less back-reflection at the tropopause in the compressible case. But at short times there is a very noticeable discrepancy because the compressible curves show a clear signal of a wave disturbance reaching the ionosphere a mere 5–10 min after the tsunami started, which is much faster than any internal waves traveling at its group velocity. This is the very first tsunami-induced signal that reaches the ionosphere.

Our interpretation of this signal is that it is a fast acoustic precursor wave that has been generated during the nearly impulsive phase $t \le \tau$ of our tsunami model (13), when the tsunami shape $h(x, t)$ grew very quickly from zero to the prescribed shape $f(x)$. The numerical value of τ for our simulations is 10 s. This very quick displacement of the lower boundary sets off an acoustic wave in the atmosphere that travels unimpeded in the vertical. This is a very compelling interpretation, as can be seen from the snapshots in Fig. 5. The left and middle panels resemble the anelastic results in Fig. 1, with some differences, such as an increased amplitude in the compressible case. But the right panel clearly shows the fast acoustic precursor wave, which has absolutely no counterpart in the anelastic model. This makes obvious that the precursor wave is an acoustic wave.

TABLE 1. Summary of the parameters used for the effective layers, each of which represents the troposphere, the stratosphere, the mesosphere, and the uppermost layer above the mesopause, respectively.

Layer	Height at the top (km)	N (s^{-1})	H (km)	c ($m\,s^{-1}$)
Troposphere	11	0.011	9.1	320
Stratosphere	47	0.022	6.4	300
Mesosphere	80	0.017	8.1	325
Above	∞	0.023	5.3	270

5. Concluding comments

Our idealized theory and numerical examples have highlighted the importance of back-reflection at the tropopause and of compressible effects for capturing the accurate time evolution of internal acoustic–gravity waves. These waves are generated by a tsunami at the air–sea interface and then subsequently propagate rapidly in the vertical to reach the ionosphere, where they can leave a detectable fingerprint that can be picked up by remote sensing methods. Our work has been restricted to a two-dimensional vertical slice model for the atmosphere, but there are no particular challenges that need to be overcome if one wanted to extend the approach to three-dimensional waves or, indeed, to more realistic air–sea interface shapes associated with realistic tsunamis. In all cases, the practical bottleneck will be the need to compute the inverse Laplace transform numerically, which is computationally expensive in the absence of a usable fast transform algorithm for this problem. Still, it is the power of the Laplace transform that allows us to satisfy the appropriate radiation condition exactly, so this is a price worth paying.

To incorporate a more realistic atmospheric profile, we divide the atmosphere above the tropopause into various layers. Starting with the profile corresponding to the *U.S. Standard Atmosphere, 1976*, we simplify it by grouping those layers above the tropopause with close values of N, H, and c into single layers. This way, we obtain a simplified description that includes one layer for the troposphere, one effective layer representative of the stratosphere, another layer representative of the mesosphere, and one infinite isothermal layer for everything above the mesopause. The parameters of each layer are summarized in Table 1.

The result of using this new profile is displayed in green in Fig. 4. The asymptotic steady-state limit is smaller than that of the two-layer model. This is due mainly to two causes: on the one hand, the more complex stratification profile of the atmosphere yields additional reflected waves, particularly near the mesopause. On the other hand, the uppermost isothermal layer has a more rigid profile (i.e., lower density scale height H than those in the two-layer model), so waves with the same energy have smaller amplitude. These two factors combine to decrease the amplitude of the waves transmitted into the uppermost layer.

Equation (13) of the motion of tsunami describes the deflection of the ocean's surface at the time of the earthquake as equally coherent as the wave front is expected to be after propagating a significant distance away from the source. However, we expect the initial lack of coherence of the signal not to affect the predicted acoustic response in a significant matter. That is because, at the initial stage of the acoustic precursor, the wave field is dominated by the small horizontal wavenumbers (cf. the large horizontal wavelength indicated from the black solid lines in the right panel of Fig. 5), corresponding to smooth averages over long horizontal domains. Therefore, this response is sensitive to the large-scale features of the tsunami, rather than to its small-scale details.

From a physical point of view, perhaps the most striking observable feature is the very fast acoustic precursor wave that is so clearly visible in Fig. 5. Work is currently underway to understand the dynamics of this precursor wave by using a one-dimensional acoustic model along the centerline of the tsunami location. The essence of the linear dynamics of this wave is already suggested by the compressible dispersion relation (27), which, for x-independent waves, reduces to

$$\hat{\omega}^2 = \frac{c^2}{4H^2} + c^2 m^2 . \tag{36}$$

This is a dispersive equation of the Klein–Gordon type, with group velocities bounded by the nondispersive background sound speed c at small vertical scales and slower, dispersive wave speeds associated with larger vertical scales. Presumably, the visible large-scale oscillations behind the wave pulse in Fig. 5 can be associated with the slower, dispersive components of the impulsively generated acoustic wave.

This fast acoustic precursor is a propagating sound wave. As is seen from the dispersion relation (36), for lower frequencies of tsunami perturbation (i.e., for larger τ), the acoustic precursor has a larger vertical wavelength. The amplitude of its vertical displacement does not depend on τ: For larger τ, the vertical velocity ($w \sim \tau^{-1}$) is smaller, but the time for integration of w is longer, so the vertical displacement, which is time-integrated from w, is not greatly affected.

Moreover, it seems possible that the wave pulse sharpens and forms a nonlinear shock at some time during its travel from the ground to the ionosphere at

100-km altitude. This suggests the possibility of important nonlinear effects that may affect the earliest observable tsunami fingerprint in the ionosphere. We hope to report on a detailed study of this acoustic wave precursor in the near future.

Acknowledgments. The authors gratefully acknowledge fruitful discussions and financial support under the auspices of an Office of Naval Research Basic Research Challenge (N000141310117) that funded this research.

APPENDIX A

Fourier–Laplace Transform of Lower Boundary

The Fourier transform of $h(x, t)$ in (13) is

$$\hat{h}(k,t) = \begin{cases} (t/\tau)\hat{f}(k), & 0 < t \le \tau \\ e^{-ikV(t-\tau)}\hat{f}(k), & t > \tau. \end{cases}$$

The Laplace transform of $\hat{h}(k, t)$ in t is then

$$\begin{aligned} \hat{h}^{\mathrm{T}}(k,s) &= \int_0^\infty \hat{h}(k,t)e^{-st}\,dt \\ &= \left[\int_0^\tau (t/\tau)e^{-st}\,dt + \int_\tau^\infty e^{-ikV(t-\tau)}e^{-st}\,dt\right]\hat{f}(k) \\ &= e^{-s\tau}\left[\frac{2e^{(s\tau/2)}\sinh(s\tau/2)}{s^2\tau} - \frac{1}{s} + \frac{1}{s+ikV}\right]\hat{f}(k). \end{aligned}$$

APPENDIX B

Effective Wavelength

We derive a simple effective wavelength λ_x that can be associated with a given tsunami shape $f(x)$. First, define an effective horizontal wavenumber as

$$K^* = \frac{\sum_k |k||\hat{f}(k)|^2}{\sum_k |\hat{f}(k)|^2} \quad \text{or} \quad K^* = \frac{\int |k||\hat{f}(k)|^2\,dk}{\int |\hat{f}(k)|^2\,dk} \tag{B1}$$

in the case of a discrete or a continuous spectrum, respectively. It is easy to check that in the steady lee-wave problem with uniform stratification, a sinusoidal lower boundary with wavenumber K^* and root-mean-square amplitude equal to that of $f(x)$ produces the same wave energy flux and pseudomomentum flux as $f(x)$. The effective wavelength is then defined to be $\lambda_x = 2\pi/K^*$. For the Gaussian-shaped lower boundary $f(x) = \exp(-x^2/2\sigma^2)$, this yields $K^* = (\sqrt{\pi}\sigma)^{-1}$ and $\lambda_x = 2\pi^{3/2}\sigma$.

APPENDIX C

Derivation of Pseudomomentum Flux

a. Pseudomomentum flux for anelastic gravity waves

Equation (1a) gives the relation between u and w:

$$\partial_x u + \partial_z w - \frac{w}{H} = 0, \tag{C1}$$

where H is the density scale height. Substituting the plane wave structure

$$u = \sum_k \frac{\hat{u}(k,z)}{\sqrt{\rho_0(z)}}e^{ik(x-Vt)}, \quad w = \sum_k \frac{\hat{w}(k,z)}{\sqrt{\rho_0(z)}}e^{ik(x-Vt)} \tag{C2}$$

into (C1), we obtain

$$\hat{u} = \frac{i}{k}\left(\partial_z - \frac{1}{2H}\right)\hat{w}. \tag{C3}$$

The pseudomomentum flux divided by $\rho_0(0)$ is

$$\begin{aligned} D_g &= -\overline{uw} = -\sum_k \mathrm{Re}\{\hat{u}(k,z)\hat{w}^*(k,z)\} \\ &= -\sum_k \mathrm{Re}\left\{\frac{i\hat{w}^*(k,z)[\partial_z\hat{w}(k,z) - \hat{w}/(2H)]}{k}\right\} \\ &= -\sum_k \mathrm{Re}\left\{\frac{i\hat{w}^*(k,z)\partial_z\hat{w}(k,z)}{k}\right\}. \end{aligned}$$

Substituting $\hat{w} = -ik(V - U)\hat{\zeta}$ into the above equation, we have

$$\begin{aligned} D_g &= -\sum_k \mathrm{Re}\{ik(V-U)\hat{\zeta}^*(k,z)\partial_z[(V-U)\hat{\zeta}(k,z)]\} \\ &= -\sum_k \mathrm{Re}\{ik(V-U)\hat{\zeta}^*(k,z)[(V-U)\partial_z\hat{\zeta}(k,z) - U'\hat{\zeta}(k,z)]\} \\ &= -\sum_k \mathrm{Re}\{ik(V-U)^2\hat{\zeta}^*(k,z)\partial_z\hat{\zeta}(k,z)\}. \end{aligned} \tag{C4}$$

Let us assume there is no background wind $U = 0$. Then (C4) becomes

$$\begin{aligned} D_g &= -\sum_k \mathrm{Re}\{ikV^2\hat{\zeta}^*(k,z)\partial_z\hat{\zeta}(k,z)\} \\ &= \sum_{k\in S} kV^2 m_g(k)|\hat{\zeta}(k,z)|^2, \end{aligned}$$

where the last equality follows from $\partial_z\hat{\zeta}(k, z) = im_g(k)\zeta(k, z)$, $m_g(k)$ is the vertical wavenumber from (16), and S is the set of k such that the corresponding wave modes are propagating waves.

b. Pseudomomentum flux for acoustic–gravity waves

Substituting (21a) and (21e) into (21d) to cancel ρ_1, we have

$$D_t\left(\frac{p}{\rho_0}\right) - gw + c^2(\partial_x u + \partial_z w) = 0.$$

Canceling p from (21b) and the above equation, we have

$$(D_t^2 - c^2\partial_x^2)u = (c^2\partial_{xz}^2 - g\partial_x - U'D_t)w. \qquad \text{(C5)}$$

Substituting the plane wave structure (C2) into (C5), we obtain

$$\hat{u}(k,z) = i\frac{\partial_z + 1/(2H) - g/c^2 - [(V-U)^2]'/(2c^2)}{k\{1-[(V-U)/c]^2\}}\hat{w}(k,z). \qquad \text{(C6)}$$

The pseudomomentum flux divided by $\rho_0(0)$ is

$$D = -\overline{uw} = -\sum_k \mathrm{Re}\{\hat{u}(k,z)\hat{w}^*(k,z)\} = -\sum_k \mathrm{Re}\left\{\frac{i\hat{w}^*(k,z)\partial_z\hat{w}(k,z)}{k\{1-[(V-U)/c]^2\}}\right\},$$

where, in the last equality, only $\partial_z\hat{w}$ term in (C6) survives undertaking the real part of $\hat{u}\hat{w}^*$. Substituting $\hat{w} = -ik(V-U)\hat{\zeta}$ into the above equation, we have

$$\begin{aligned} D &= -\sum_k \mathrm{Re}\left\{\frac{ik(V-U)\hat{\zeta}^*(k,z)\partial_z[(V-U)\hat{\zeta}(k,z)]}{1-[(V-U)/c]^2}\right\} \\ &= -\sum_k \mathrm{Re}\left\{\frac{ik(V-U)\hat{\zeta}^*(k,z)[(V-U)\partial_z\hat{\zeta}(k,z) - U'\hat{\zeta}(k,z)]}{1-[(V-U)/c]^2}\right\} \\ &= -\sum_k \mathrm{Re}\left\{\frac{ik(V-U)^2\hat{\zeta}^*(k,z)\partial_z\hat{\zeta}(k,z)}{1-[(V-U)/c]^2}\right\}. \end{aligned} \qquad \text{(C7)}$$

Let us assume there is no background wind $U = 0$. Then (C7) becomes

$$\begin{aligned} D &= -\sum_k \mathrm{Re}\left\{\frac{ikV^2\hat{\zeta}^*(k,z)\partial_z\hat{\zeta}(k,z)}{1-(V/c)^2}\right\} \\ &= \sum_{k\in S}\frac{kV^2 m(k)|\hat{\zeta}(k,z)|^2}{1-(V/c)^2}, \end{aligned} \qquad \text{(C8)}$$

where $m(k)$ is the vertical wavenumber from (35), and S is the set of k such that the corresponding wave modes are propagating waves.

Equation (C8) of pseudomomentum flux is consistent with the work–energy relation where the power of the mean drag exerted by the tsunami shape on the atmosphere above (which equals D) balances the mean wave energy flux. Indeed, according to Lighthill (1978, 297–298), the mean vertical energy flux generated by a sinusoidal lower boundary with wavenumber k is

$$\frac{\omega m(k)|w|^2}{k^2-(\omega/c)^2} = \frac{\omega m(k)|\hat{w}(k,z)|^2}{k^2-(\omega/c)^2} = \frac{\omega^3 m(k)|\hat{\zeta}(k,z)|^2}{k^2-(\omega/c)^2},$$

where the last equality follows from $\hat{w}(k,z) = -i\omega\hat{\zeta}(k,z)$, and ω is the intrinsic frequency. For waves induced by a multichromatic lower boundary, the mean vertical energy flux is the sum of monochromatic energy fluxes:

$$\mathscr{F} = \sum_{k\in S}\frac{\omega^3 m(k)|\hat{\zeta}(k,z)|^2}{k^2-(\omega/c)^2} = \sum_{k\in S}\frac{kV^3 m(k)|\hat{\zeta}(k,z)|^2}{1-(V/c)^2},$$

where we have substituted $\omega = kV$ in the last equality. Substituting (C8) into the above equation, we recover the work–energy relation:

$$DV = \sum_{k\in S}\frac{kV^3 m(k)|\hat{\zeta}(k,z)|^2}{1-(V/c)^2} = \mathscr{F}.$$

APPENDIX D

Instantaneous Response of Anelastic-Gravity Waves in the Stratosphere

We compute the structure of the instantaneous response of the anelastic wave field to an impulsively deformed lower boundary. This response is nonzero but decays exponentially with altitude. From the definition of the Laplace transform, the instantaneous response at $t\to 0+$ is given by

$$\begin{aligned} &\lim_{t\to 0+}\hat{\zeta}_2(k,z,t) \\ &\quad = \lim_{s\to\infty} s\hat{\zeta}_2^{\mathrm{T}}(k,z,s) \\ &\quad = \lim_{s\to\infty}\frac{\sqrt{\rho_0(0)}[s\hat{h}^{\mathrm{T}}(k,s)]e^{-\lambda_2(k,s)(z-z_p)}}{\mu(k,s)\sinh[\lambda_1(k,s)z_p] + \cosh[\lambda_1(k,s)z_p]}. \end{aligned}$$

The z dependence is included only in the $e^{-\lambda_2(k,s)(z-z_p)}$ term. From (10a), we have

$$\lim_{s\to\infty}\lambda_2(k,s) = \sqrt{k^2 + \frac{1}{4H_2^2}}, \qquad \text{(D1)}$$

so the instantaneous response of the rescaled wave field in the stratosphere exponentially decays with the rate (D1) provided $\lim_{s\to\infty}|s\hat{h}^{\mathrm{T}}(k,s)| < \infty$. So the instantaneous response of the physical wave field

$[\hat{\zeta}_2/\sqrt{\rho_0(z)}]$ in the stratosphere exponentially decays with the rate

$$\lim_{s\to\infty}\lambda_2(k,s)-\frac{1}{2H_2}=\sqrt{k^2+\frac{1}{4H_2^2}}-\frac{1}{2H_2}>0. \quad \text{(D2)}$$

REFERENCES

Artru, J., V. Ducic, H. Kanamori, P. Lognonné, and M. Murakami, 2005: Ionospheric detection of gravity waves induced by tsunamis. *Geophys. J. Int.,* **160,** 840–848, doi:10.1111/j.1365-246X.2005.02552.x.

Bannon, P. R., 1996: On the anelastic approximation for a compressible atmosphere. *J. Atmos. Sci.,* **53,** 3618–3628, doi:10.1175/1520-0469(1996)053<3618:OTAAFA>2.0.CO;2.

Brančík, L., 2011: Numerical inverse Laplace transforms for electrical engineering simulation. *MATLAB for Engineers—Applications in Control, Electrical Engineering, IT and Robotics,* K. Perutka, Ed., InTech, 51–74.

Chumakova, L. G., R. R. Rosales, and E. G. Tabak, 2013: Leaky rigid lid: New dissipative modes in the troposphere. *J. Atmos. Sci.,* **70,** 3119–3127, doi:10.1175/JAS-D-12-065.1.

COESA, 1976: *U.S. Standard Atmosphere, 1976.* NOAA, 227 pp.

Hines, C. O., 1972: Gravity waves in the atmosphere. *Nature,* **239,** 73–78, doi:10.1038/239073a0.

Lighthill, J., 1978: *Waves in Fluids.* Cambridge University Press, 504 pp.

Lipps, F. B., 1990: On the anelastic approximation for deep convection. *J. Atmos. Sci.,* **47,** 1794–1798, doi:10.1175/1520-0469(1990)047<1794:OTAAFD>2.0.CO;2.

Makela, J. J., and Coauthors, 2011: Imaging and modeling the ionospheric airglow response over Hawaii to the tsunami generated by the Tohoku earthquake of 11 March 2011. *Geophys. Res. Lett.,* **38,** L00G02, doi:10.1029/2011GL047860.

Nappo, C. J., 2002: *An Introduction to Atmospheric Gravity Waves,* International Geophysics Series, Vol. 85, Academic Press, 279 pp.

Occhipinti, G., E. A. Kherani, and P. Lognonné, 2008: Geomagnetic dependence of ionospheric disturbances induced by tsunamigenic internal gravity waves. *Geophys. J. Int.,* **173,** 753–765, doi:10.1111/j.1365-246X.2008.03760.x.

——, P. Coïsson, J. J. Makela, S. Allgeyer, A. Kherani, H. Hébert, and P. Lognonné, 2011: Three-dimensional numerical modeling of tsunami-related internal gravity waves in the Hawaiian atmosphere. *Earth Planets Space,* **63,** 847–851, doi:10.5047/eps.2011.06.051.

Peltier, W. R., and C. O. Hines, 1976: On the possible detection of tsunamis by a monitoring of the ionosphere. *J. Geophys. Res.,* **81,** 1995–2000, doi:10.1029/JC081i012p01995.

Rolland, L. M., G. Occhipinti, P. Lognonné, and A. Loevenbruck, 2010: Ionospheric gravity waves detected offshore Hawaii after tsunamis. *Geophys. Res. Lett.,* **37,** L17101, doi:10.1029/2010GL044479.

Shapiro, A. H., 1953: *The Dynamics and Thermodynamics of Compressible Fluid Flow.* Vol. 1. Ronald Press, 647 pp.